# A new proposal for urease mechanism based on the crystal structures of the native and inhibited enzyme from *Bacillus pasteurii*: why urea hydrolysis costs two nickels

Stefano Benini[1], Wojciech R Rypniewski[1], Keith S Wilson[2], Silvia Miletti[3], Stefano Ciurli[3]* and Stefano Mangani[4]*

**Background:** Urease catalyzes the hydrolysis of urea, the final step of organic nitrogen mineralization, using a bimetallic nickel centre. The role of the active site metal ions and amino acid residues has not been elucidated to date. Many pathologies are associated with the activity of ureolytic bacteria, and the efficiency of soil nitrogen fertilization with urea is severely decreased by urease activity. Therefore, the development of urease inhibitors would lead to a reduction of environmental pollution, to enhanced efficiency of nitrogen uptake by plants, and to improved therapeutic strategies for treatment of infections due to ureolytic bacteria. Structure-based design of urease inhibitors would require knowledge of the enzyme mechanism at the molecular level.

**Results:** The structures of native and inhibited urease from *Bacillus pasteurii* have been determined at a resolution of 2.0 Å by synchrotron X-ray cryogenic crystallography. In the native enzyme, the coordination sphere of each of the two nickel ions is completed by a water molecule and a bridging hydroxide. A fourth water molecule completes a tetrahedral cluster of solvent molecules. The enzyme crystallized in the presence of phenylphosphorodiamidate contains the tetrahedral transition-state analogue diamidophosphoric acid, bound to the two nickel ions in an unprecedented mode. Comparison of the native and inhibited structures reveals two distinct conformations of the flap lining the active-site cavity.

**Conclusions:** The mode of binding of the inhibitor, and a comparison between the native and inhibited urease structures, indicate a novel mechanism for enzymatic urea hydrolysis which reconciles the available structural and biochemical data.

Addresses: [1]European Molecular Biology Laboratory, DESY, Notkestraße 85, D-22603 Hamburg, Germany, [2]Department of Chemistry, University of York, Heslington, York YO1 5DD, United Kingdom, [3]Institute of Agricultural Chemistry, University of Bologna, Viale Berti Pichat 10 I-40127 Bologna, Italy and [4]Department of Chemistry, University of Siena, Pian dei Mantellini, 44 I-53100 Siena, Italy.

*Corresponding authors.
E-mail: sciurli@agrsci.unibo.it
mangani@unisi.it

**Key words:** *Bacillus pasteurii*, diamidophosphate, phenylphosphorodiamidate, urease, X-ray structure

Received: **30 September 1998**
Revisions requested: **29 October 1998**
Revisions received: **24 November 1998**
Accepted: **4 December 1999**

Published: **1 February 1999**

**Structure** February 1999, **7**:205–216
http://biomednet.com/elecref/0969212600700205



## Introduction

The recent determination of the X-ray structure of urease from a bacterial source, *Klebsiella aerogenes* [1,2], has provided the first three-dimensional structural model of the enzyme, a key step towards the understanding of the catalytic mechanism. In the active site of native *K. aerogenes* urease (KAU), two nickel ions are held at a separation of 3.6 Å by the bridging carboxylate group of a carbamylated lysine residue [1]. Both ions are further coordinated by two histidines, while one of them is also bound to an aspartate. In the first structural model reported (2.2 Å resolution, 92% completeness, R factor = 18.2%, PDB code 1KAU) [1], a disordered water molecule was proposed to bind the two metal ions asymmetrically. This model suggested two different coordination geometries for the nickel ions: one tri-coordinated pseudotetrahedral (with low occupancy of the fourth site by a water molecule); the other penta-coordinated distorted trigonal bipyramidal (with incomplete occupancy of a coordination site by a water molecule).

This structural model for the active site of native KAU was in conflict with all previous spectroscopic data on ureases from *K. aerogenes* [3] and from jack bean (*Canavalia ensiformis*) [3–9], which had indicated the presence of hexa- or penta-coordinated slightly distorted octahedral nickel ions. It has been remarked that the inconsistencies between the spectroscopic and structural analyses could be resolved by the presence of low molecular weight, non-protein ligands in the vicinity of the metal ions, possibly water molecules or hydroxide ions bound to the nickel centers either in an end-on or a bridging mode [10]. These were not detected in the first model of KAU, because of the relatively low resolution and lack of completeness of the diffraction data [1]. The solution of this conflict is extremely important for understanding the catalytic mechanism of urea hydrolysis, for which the role of water molecules (or hydroxide ions) in the active site is crucial [11]. The location of water molecules in the active site of KAU has been the subject of intense discussions [2,12]. In the most recent model proposed for KAU (2.2 Å resolution, completeness

not reported, R factor = 17.3%, PDB code 1FWJ), the additional electron density found in the neighborhood of the nickel ions was suggested to be water molecules in sites that are only partially occupied, because the oxygen–oxygen distances between them (2.0–2.5 Å) were considered too short to fully occupy the sites [2,12]. Therefore the presence and position of solvent molecules bound to the nickel center remained ambiguous.

In order to tackle the 'water problem' for the active site of this hydrolytic metallo-enzyme and to contribute to the understanding of its catalytic and inhibition mechanisms, urease from *Bacillus pasteurii*, a highly ureolytic soil bacterium, was purified [13] and crystallized [14]. *B. pasteurii* urease (BPU) is heteropolymeric [13] ($M_r(\alpha) = 61.4$ kDa; $M_r(\beta) = 14.0$ kDa; $M_r(\gamma) = 11.1$ kDa [15]) and features an active site containing two nickel ions [13]. The primary structures of BPU [15] and KAU [16] are highly homologous (63% (α), 46% (β) and 61% (γ), respectively), and the amino acid residues ligating the nickel ions are conserved [15]. Ni-edge X-ray absorption spectroscopy (XAS) studies, carried out on BPU, suggest an average coordination environment of the pseudo-octahedral nickel ions made of five or six nitrogen or oxygen ligands, with two of the ligands being histidine imidazole sidechains [10]. Synchrotron X-ray cryogenic data collection for BPU, both in the native form and inhibited with β-mercaptoethanol (β-ME), has been reported [14], while the structure and binding mode of β-ME to the active site (1.65 Å resolution, 98.7% completeness, R factor = 16%, PDB code 1UBP) has recently been described [17].

This account presents a detailed three-dimensional structure of native BPU, finally showing a clear picture of the water/hydroxide molecules in the active site, together with the structure of the enzyme crystallized in the presence of phenylphosphorodiamidate $(NH_2)_2PO(OPh)$, PPD, a well-known urease inhibitor [18–21], showing the presence of diamidophosphoric acid $(NH_2)_2PO(OH)$, DAP, bound to the nickel ions in the active site. The present results yield information on the structure of BPU in the resting state and bound to a transition-state analogue, and provide strong support for the formulation of a novel catalytic mechanism of enzymatic urea hydrolysis.

## Results and discussion

### Urease architecture and topology

BPU is an heteropolymeric molecule $(\alpha\beta\gamma)_3$ with exact threefold symmetry (Figure 1), as four urease molecules lie on the 'special' positions of point symmetry 3 present in the $P6_322$ hexagonal cell. In both native and inhibited BPU, the protein backbone of the three subunits closely matches both the secondary and the tertiary structures found in KAU. The α subunit consists of an $(\alpha\beta)_8$ barrel domain and a β-type domain. The β subunit, located on the external surface of the trimer, is predominantly β structure,

**Figure 1**

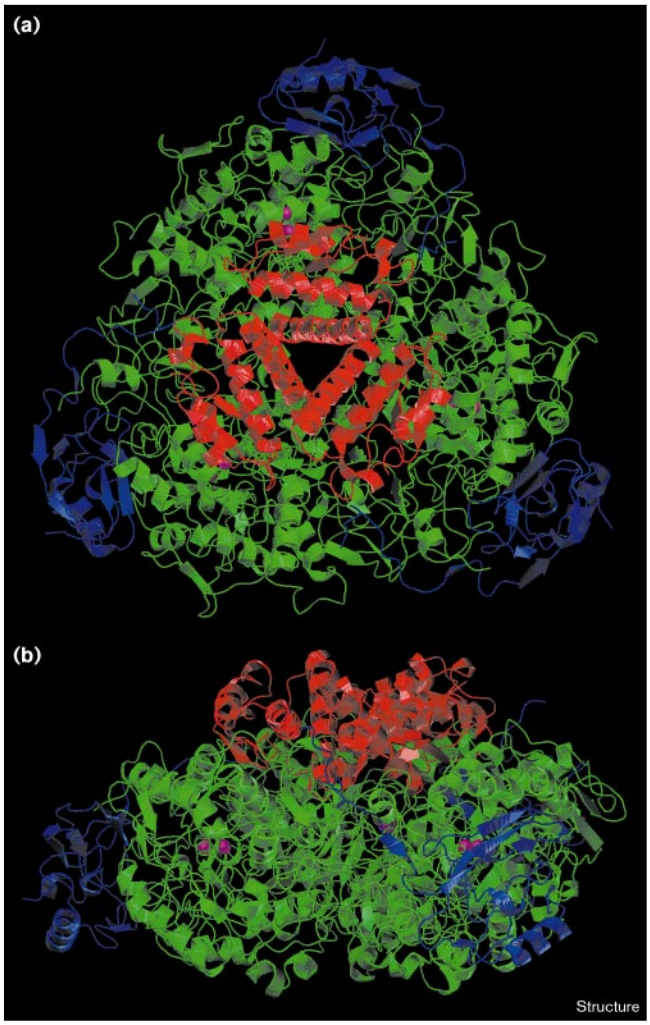


Ribbon diagram of the $(\alpha\beta\gamma)_3$ heterotrimer of BPU. **(a)** View down the crystallographic threefold axis; **(b)** view from the side. The green, blue and red ribbons represent, respectively, the α, β and γ subunits. The magenta spheres in the α subunits are the nickel ions of the active center.

but features an additional C-terminal α helix of 12 amino acids (109–120; the BPU consensus sequence will be used hereafter), not found in KAU, which does not interact with the other subunits. The three γ subunits consist of αβ domains located on top of each pair of α subunits, thereby favouring their association into a trimer.

The biggest conformational change between native BPU and KAU occurs in the helix–turn–helix motif (residues 311–340) of the α subunit, lining the active-site cleft. In KAU, this motif is characterized by high mobility as judged by the temperature factors [12]; this mobility is proposed to be important for regulating both the access of the substrate to the active site and the release of the reaction products

**Figure 2**

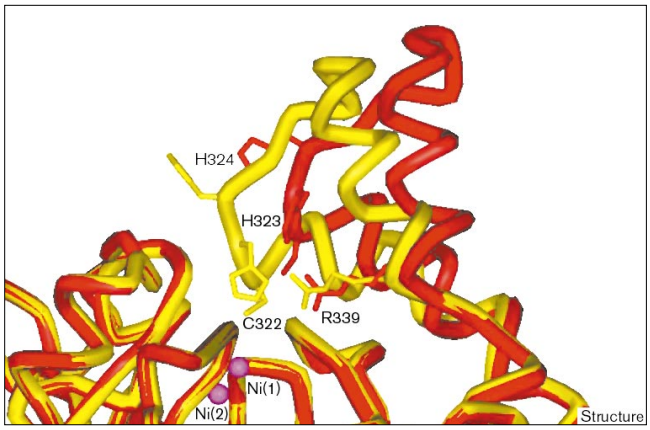


Different conformations adopted by the helix–turn–helix motif of the flexible flap in BPU. The native form is shown in red and the DAP complex in yellow. The sidechains of the residues experiencing large movements between the two flap states are shown as stick models and labelled. The two nickel ions of the native enzyme are shown as purple spheres of arbitrary radius.

**Figure 3**

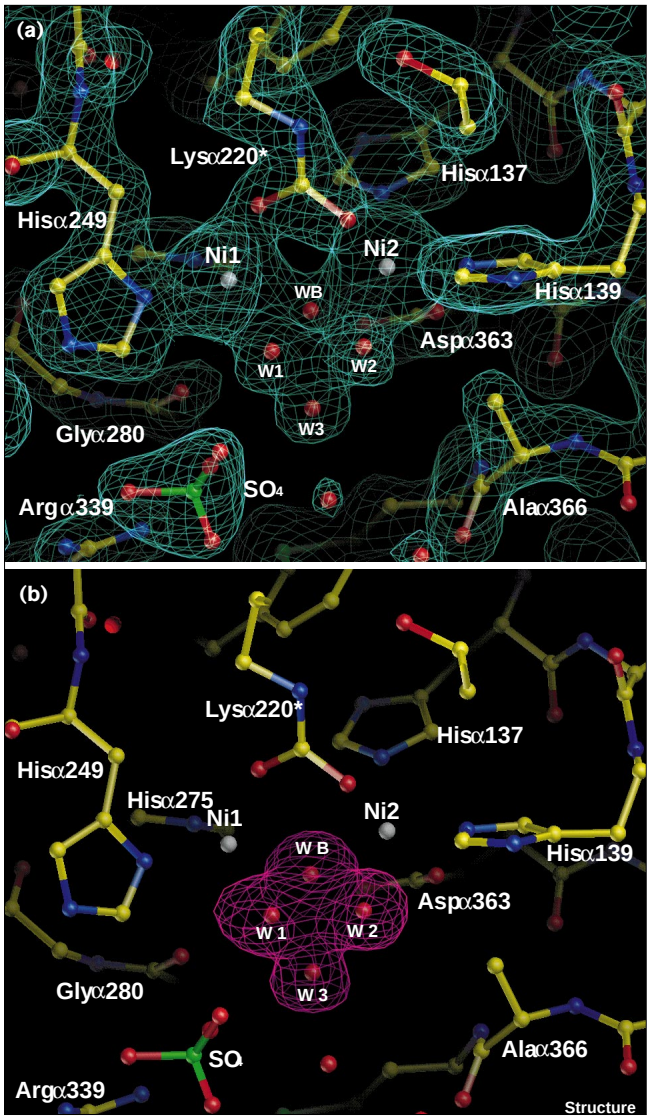


The active site of BPU. **(a)** Atomic model of the active site of native BPU. The nickel coordination environment is shown superimposed on the final $2F_o–F_c$ electron-density map contoured at 1σ. **(b)** Omit map. The active-site water cluster is shown as calculated with Fourier coefficients $F_o–F_c$ and phases derived from the final model from which the oxygen atoms corresponding to W(1), W(2), W(3) and W(B) had been removed (purple map, contoured at 4σ). Carbon, nitrogen, oxygen and sulphur atoms are shown in yellow, blue, red and green, respectively; the nickel ions are in grey.

[1,22]. The motif thereby acts as a 'flap', and shows large displacement parameters also in native BPU, but has a significantly different conformation compared with native KAU [1]. In particular, the flap can be considered to be in an 'open' conformation as opposed to the 'closed' conformation in KAU. In contrast, in BPU crystallized in the presence of PPD, the flap is in the 'closed' conformation, very similar to that found in native KAU (Figure 2). In BPU inhibited with β-ME, the flap is 'open' [17], as is also found in the Cys$^{\alpha 319}$Tyr mutant of KAU [12]. The various structural data, therefore, indicate the existence of two distinct conformations of the flap. The amino acid sequence of the helix–turn–helix motif of the flap in BPU and KAU is conserved in the first and second helices (except for an Asp/Glu substitution), but not in the loop, which changes from Asp–Pro–Asp in KAU to Lys–Asn–Asn in BPU. Clearly, the loop sequence identity is not necessary for flexibility. In contrast, the regions of the structure that act as the fulcrum of the conformational change (residues 306–310 and 341–348) are highly conserved.

### Active site of native BPU

In BPU, each α subunit hosts an active site characterized by the presence of a binuclear nickel center. Each active site is separated from the other by 51 Å. The metal ions are located roughly half-way down a 15 Å deep active-site cleft (Figure 2). The electron density in the active site is very well defined, providing a clear picture of the nickel coordination (Figure 3a). The two nickel ions are bridged by the carboxylate group of the carbamylated Lys$^{\alpha 220*}$, (where the asterisk denotes the fact that the lysine residue is unconventional in the sense that the $NH_2$ group is carbamylated) bound to Ni(1) through Oθ1 and to Ni(2) through Oθ2. Ni(1) is further coordinated by His$^{\alpha 249}$ Nδ and His$^{\alpha 275}$ Nε, while Ni(2) is bound to His$^{\alpha 137}$ Nε, His$^{\alpha 139}$ Nε, and Asp$^{\alpha 363}$ Oδ1 (Table 1). Both nickel ions are well ordered (B factors of 19.1 and 17.9 Å$^2$ for Ni(1) and Ni(2), respectively) and the two are separated by 3.7 Å. This distance is significantly longer than for β-ME-inhibited BPU (3.1 Å) [17], and is very close to that found in native KAU (3.6 Å) [1,12].

**Table 1**

**Selected distances and angles around the Ni centers in ureases.**

| | Native BPU | DAP-inhibited BPU | Native KAU [12] |
|---|---|---|---|
| **Nickel–ligand distances (Å)** | | | |
| Ni(1)–Lys$^{\alpha 220*}$Oθ1 * | 2.1 | 2.1 | 2.1 |
| Ni(1)–$O_B$ † | 2.1 | 2.3 | 2.2 |
| Ni(1)–$O_T$ ‡ | 2.2 | 2.2 | 2.1 |
| Ni(1)–His$^{\alpha 249}$Nδ | 2.2 | 2.0 | 2.0 |
| Ni(1)–His$^{\alpha 275}$Nε | 2.2 | 2.1 | 2.3 |
| Ni(2)–Lys$^{\alpha 220*}$Oθ2 | 2.1 | 1.9 | 2.1 |
| Ni(2)–$O_B$ | 2.2 | 2.3 | 2.0 |
| Ni(2)–$O_T$ ($N_T$) | 2.1 | 2.3 | 2.1 |
| Ni(2)–His$^{\alpha 137}$Nε | 2.2 | 2.1 | 2.3 |
| Ni(2)–His$^{\alpha 139}$Nε | 2.2 | 2.2 | 2.2 |
| Ni(2)–Asp$^{\alpha 363}$Oδ1 | 2.2 | 2.1 | 2.2 |
| Ni(1)–Ni(2) | 3.7 | 3.8 | 3.6 |
| **Ligand–nickel–ligand angles (°)** | | | |
| Lys$^{\alpha 220*}$Oθ1–Ni(1)–His$^{\alpha 249}$Nδ | 105 | 111 | 94 |
| Lys$^{\alpha 220*}$Oθ1–Ni(1)–His$^{\alpha 275}$Nε | 111 | 106 | 106 |
| Lys$^{\alpha 220*}$Oθ1–Ni(1)–$O_T$ | 104 | 103 | 104 |
| Lys$^{\alpha 220*}$Oθ1–Ni(1)–$O_B$ | 95 | 95 | 97 |
| His$^{\alpha 249}$Nδ–Ni(1)–His$^{\alpha 275}$Nε | 95 | 103 | 92 |
| $O_T$–Ni(1)–$O_B$ | 58 | 67 | 72 |
| $O_T$–Ni(1)–His$^{\alpha 275}$Nε | 140 | 143 | 150 |
| Lys$^{\alpha 220*}$Oθ2–Ni(2)–His$^{\alpha 137}$Nε | 94 | 90 | 90 |
| Lys$^{\alpha 220*}$Oθ2–Ni(2)–His$^{\alpha 139}$Nε | 88 | 94 | 92 |
| Lys$^{\alpha 220*}$Oθ2–Ni(2)–$O_T$ ($N_T$) | 91 | 99 | 103 |
| His$^{\alpha 137}$Nε–Ni(2)–His$^{\alpha 139}$Nε | 113 | 108 | 110 |
| ($N_T$) $O_T$–Ni(2)–$O_B$ | 63 | 71 | 59 |
| Lys$^{\alpha 220*}$Oθ2–Ni(2)–Asp$^{\alpha 363}$Oδ1 | 175 | 168 | 171 |
| Ni(1)–$O_B$–Ni(2) | 119 | 110 | 121 |

*BPU consensus sequence. †The suffix B indicates the bridging atom. ‡The suffix T indicates the terminal atom.

The difference Fourier maps unambiguously show a tetrahedrally shaped volume of electron density located towards the open side of the active-site cleft in the vicinity of the two nickel ions. This density is symmetrically positioned between the metal centers, and suggests the presence of non-protein ligands completing the metal coordination spheres. Several attempts to interpret this density involved the fitting and refining of phosphate or sulphite (present in the purification buffers), and sulphate or tetraaquo-lithium (present in the precipitant solution): the first three cases were dismissed because of the low electron density in the center of the tetrahedron, insufficient for either sulphur or phosphorous, whereas for tetraaquo-lithium the alkali metal ion could be placed in the central density only by restraining its position. The resulting Li–O distances, however, refined to very short values (~1.5 Å) compared with those found in small-molecule structures of the lithium tetraaquo ion (1.85–2.05 Å) [23].

The best model, completely accounting for the tetrahedral density as evidenced in the omit map shown in Figure 3b, entails four well-ordered water/hydroxide molecules — W(1), W(2), W(3) and W(B) — (B factors 16.8–22.8 Å$^2$). One of these (W(B)) symmetrically bridges the two nickel ions, whereas W(1) and W(2) complete the coordination polyhedron around the nickel ions: distorted square-pyramidal for Ni(1) and distorted octahedral for Ni(2). The basal plane of the Ni(1) square pyramid consists of His$^{\alpha 275}$ Nε, His$^{\alpha 249}$ Nδ, W(1) and W(B), the apical ligand being the Oθ1 atom of the bridging carbamylated Lys$^{\alpha 220*}$ (Figure 4). A fourth water molecule, W(3), is found close to W(B) (at 2.3 Å), W(1) (at 2.2 Å) and W(2) (at 2.4 Å).

The $pK_a$ of a water bound to the $Ni^{2+}$ hexaaquo ion is 10.6 [24], suggesting the assignment of the protonation state of W(1) and W(2) at the optimum pH for BPU activity (pH 8.0 [25]) as water molecules. In water-bridged bimetallic complexes, the first $pK_a$ for the bridging water decreases significantly to very acidic values, while the $pK_a$ for hydroxide deprotonation is slightly lower than the $pK_a$ of the first ionization of a single ion bound to water [24]. The estimated $pK_a$ for the deprotonation of the Ni bridging hydroxide (~9–10) suggests that, at pH 8.0, W(B) is in the hydroxo form. In this context, W(B) is at hydrogen-bonding distance from Asp$^{\alpha 363}$ Oδ2 (2.5 Å) (Figure 4a). Overall, two different types of ligands bridge the binuclear nickel cluster (the carboxylate group of the carbamylated lysine and the hydroxide molecule), accounting for the observation of weak antiferromagnetic coupling [7]. The increase of the antiferromagnetic coupling constant observed above pH 9 [26] can be explained by the deprotonation of the bridging hydroxide to the oxide form, which mediates a more efficient magnetic interaction than hydroxide.

W(1) is at 2.9 Å from His$^{\alpha 222}$ Nε, which is protonated and acts as a hydrogen-bonding donor, as deduced from the interaction of His$^{\alpha 222}$ Nδ with the peptide NH group of Asp$^{\alpha 224}$ (at 2.9 Å) (Figure 4b). Meanwhile, W(2) forms a strong hydrogen bond with Ala$^{\alpha 170}$ O (at 2.9 Å), which acts as hydrogen-bonding acceptor (Figure 4b). The distances between W(B), W(1), and W(2) are short (2.1–2.2 Å) as compared with the usual interatomic distance in a regular octahedral $[Ni(H_2O)_6]^{2+}$ ion (~2.9 Å) [23]. This can be explained by assuming the presence of a four-centered hydrogen-bonding network involving a proton located in the center of the tetrahedron constituted by W(1), W(2), W(3) and W(B), as shown in Figure 4b. In this scheme, the orientation of the hydrogen atom of the bridging hydroxide is dictated by the position of the two nickel ions and of Asp$^{\alpha 363}$ Oδ2, such that a lone pair points towards the center of the tetrahedron. At the same time, the role of hydrogen-bonding donor and acceptor played by His$^{\alpha 222}$ Nε and Ala$^{\alpha 170}$ O, respectively, coupled with their directionality and with the orientation of the W(1)–Ni(1) and W(2)–Ni(2) coordination bonds, drives a proton on W(1) and a lone pair on W(2) towards the center of the tetrahedron. Finally, W(3) could use one of its available lone pairs to complete the four-centered hydrogen-bonding network, as also supported by the orientation of a hydrogen bond between W(3)

**Figure 4**

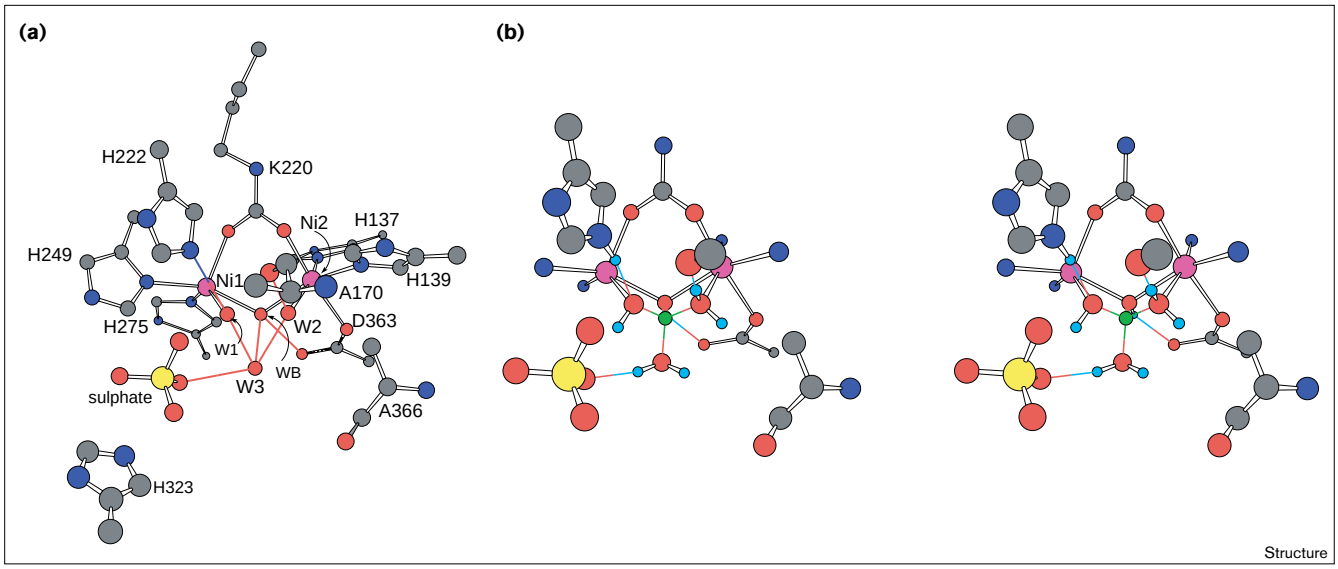


Refined model of the active site of native BPU (color scheme: carbon, grey; nitrogen, blue; oxygen, red; sulphur, yellow; hydrogen, cyan). **(a)** The different coordination environments of the two nickel ions (magenta spheres) are clearly evident. **(b)** Stereoview of the active site hydrogen-bonding network. Explicit hydrogen atoms are shown in positions that were calculated taking into account the geometric constraints, determined by the structure, on the oxygen atoms. The hydrogen atom in the center of the tetrahedral water/hydroxide molecule cluster is show in green. The proposed hydrogen bonds are coloured according to the donor–acceptor CPK colour code.

and the oxygen atom of a sulphate ion found in the cavity (Figures 3 and 4). The sulphate ion is located between the four-water/hydroxide cluster and the nearby $Arg^{\alpha 339}$, in a position occupied, in native KAU, by the imidazole ring of $His^{\alpha 323}$. $Arg^{\alpha 339}$ extends from the very bottom of the active-site cleft, and forms a strong salt bridge with the sulphate ion, which in turn forms a hydrogen bond with $His^{\alpha 323}$ Nε (at 2.7 Å). The presence of sulphate is probably due to its high concentration in the crystallization buffer. The crystals of KAU were also obtained from sulphate-rich solutions, but none of the published structures shows sulphate binding [1,2,12,22,27,28]. W(3) is at the center of additional possible multiple hydrogen-bonding interactions, being 3.3 Å from $Asp^{\alpha 363}$ Oδ2, 3.4 Å from $Gly^{\alpha 280}$ O, and 2.7 Å from a disordered water molecule situated towards the opening of the active-site cleft (Figure 3).

Using the protonation scheme reported in Figure 4b, and considering the O–O distances observed, it can be calculated that the four O–H distances within the tetrahedral cluster of solvent molecules are between 1.3 and 1.4 Å. These values agree well with the very short hydrogen-bonding distances (1.2–1.5 Å) expected for charge-assisted hydrogen bonds [29] as in our case, where a hydroxide ion is present in the hydrogen-bond network. In conclusion, the hydrogen-bonding network just described can rationalize the short O–O distances found in the active site of BPU. A further justification is provided by a detailed analysis of the interactions between W(1) or W(2) and the amino acids facing the active-site cavity, which reveals the presence of close van der Waals contacts between W(1) and $His^{\alpha 249}$ Cε (3.5 Å), $His^{\alpha 249}$ Nδ (3.2 Å), $Gly^{\alpha 280}$ O (3.7 Å), and $Lys^{\alpha 220*}$ Oθ1 (3.4 Å), and between W(2) and $His^{\alpha 139}$ Cε (3.2 Å), $His^{\alpha 139}$ Nε (3.0 Å), $Ala^{\alpha 366}$ Cβ (3.3 Å) and $Lys^{\alpha 220*}$ Oθ2 (3.0 Å) (Figure 5). The figure shows that W(1), W(2), and W(3) are highly exposed to the solvent. Furthermore, their positions roughly correspond to the molecular shape and dimension of a urea molecule.

### The active site of inhibited BPU

Figure 6a shows the electron density in the active site of BPU crystallized in the presence of PPD. The positions of all nickel-bound protein residues do not differ significantly from the structure of the native enzyme (Table 1). The electron density reveals the presence of a tetrahedrally shaped molecule bound to the dinickel centre through three atoms: one symmetrically bridges the two nickel ions, while each of the other two binds one nickel. The tetrahedral molecule has precisely replaced the cluster of four water/hydroxide molecules found in native BPU. Clearly, the bound inhibitor is not PPD, because there is no electron density for an aromatic ring. Evidence that, in the presence of PPD, the actual inhibitor is the tetrahedral diamidophosphate $(NH_2)_2PO_2^-$ (DAP), produced by the enzymatic hydrolysis of PPD to yield phenol, was previously suggested by kinetic experiments [30]. DAP was therefore used to model the density found in the inhibited BPU (Figure 6b).

**Figure 5**

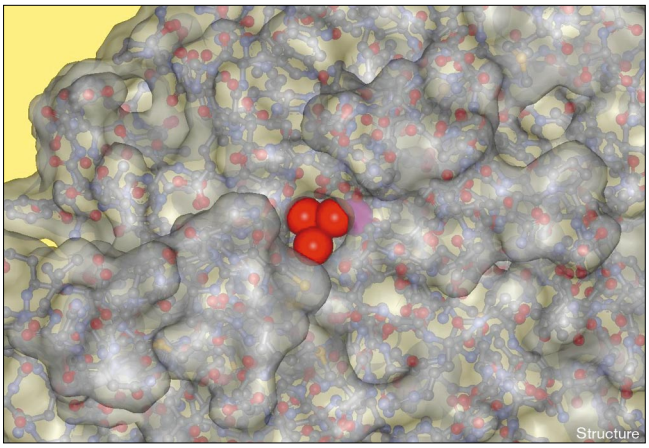


Surface of the active-site cavity of native BPU; the view from the cavity opening. The nickel ions are represented by purple spheres of 1.24 Å radius. The water molecules in the bimetallic centre are represented as small red spheres, their size corresponding to their van der Waals radius. The protein surface has been drawn with a probe sphere of 1.4 Å. The figure shows the nickel ions deeply embedded in the protein, and the close contacts between W(1), W(2) and W(3) and the sidechains of the residues shaping the active site.

**Figure 6**

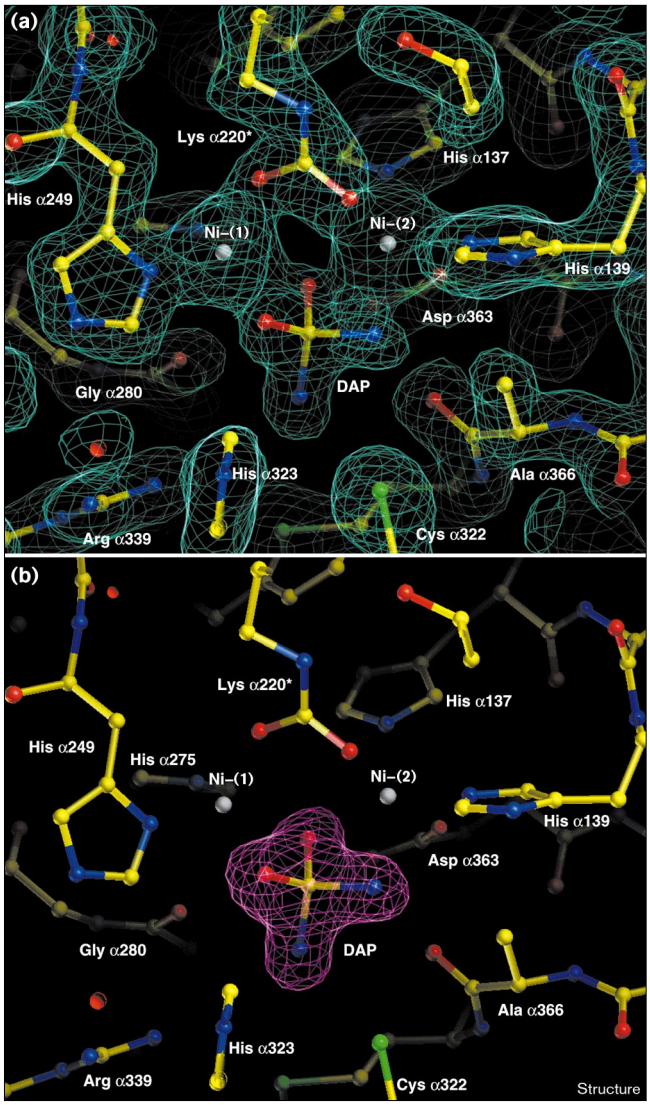


The active site of DAP-inhibited BPU. **(a)** Atomic model of the active site of DAP-inhibited BPU. The nickel coordination sphere is shown superimposed on the final $2F_o–F_c$ electron-density map (green) contoured at 1σ. **(b)** Omit map. The DAP ligand is shown as calculated with Fourier coefficients $F_o–F_c$ and phases derived from the final model from which the atoms of DAP had been removed (magenta map, contoured at 4σ).

Figure 7 shows how a remarkably specific hydrogen-bonding pattern stabilizes the inhibitor and directs its orientation in the cavity, allowing us to unambiguously assign all DAP atoms to either oxygen or nitrogen. DAP is bound to Ni(1) and to Ni(2) through one oxygen and one nitrogen atom, respectively. The second DAP oxygen atom symmetrically bridges the two nickel ions, while the second nitrogen atom points away towards the cavity opening (Figure 7a). Selected distances and angles are given in Table 1. The structure is consistent with EXAFS data previously reported on PPD-inhibited BPU [10]. As shown in Figure 7b, the Ni(1)-bound DAP oxygen atom receives a hydrogen bond from $His^{\alpha222}$ Nε (at 2.6 Å), the protonation state of which is determined, as in the native enzyme, by the interaction of $His^{\alpha222}$ Nδ with the peptide NH group of $Asp^{\alpha224}$. In contrast, the Ni(2)-bound DAP amido nitrogen forms two hydrogen bonds, donated to the carbonyl oxygen atoms of $Ala^{\alpha170}$ (at 2.9 Å) and $Ala^{\alpha366}$ (at 2.8 Å). Furthermore, the nickel-bridging DAP oxygen atom is at hydrogen-bonding distance from $Asp^{\alpha363}$ Oδ2 atom (2.5 Å), implying the presence of a proton on the bridging DAP oxygen and revealing that the actual bound inhibitor is the neutral diamidophosphoric acid $(NH_2)_2PO(OH)$. Finally, the distal DAP nitrogen donates a bifurcated hydrogen bond to $Ala^{\alpha366}$ carbonyl oxygen (3.1 Å) and to $His^{\alpha323}$ Nε (3.3 Å). The distal DAP nitrogen is within contact distance of $Asp^{\alpha363}$ Oδ2 (3.5 Å). It is remarkable that the orientation of the protons on DAP, as dictated by the structure (Figure 7b), parallels very closely the protonation scheme suggested for the water/hydroxide molecules tetrahedral cluster (Figure 4b). It is interesting to notice that, in native BPU, the proton on W(2) that is not involved in the hydrogen bond with $Ala^{\alpha170}$ (Figure 4b) points in the same direction as the corresponding proton on the DAP nitrogen atom bound to Ni(2) (Figure 7b); in the latter case this proton is involved in a hydrogen-bonding interaction with $Ala^{\alpha366}$, made possible by the closing of the flap, which induces a conformational change on the carbonyl group of $Ala^{\alpha366}$. In the same way, the protons on W(3) in native BPU are easily placed in an orientation corresponding to that expected for

**Figure 7**

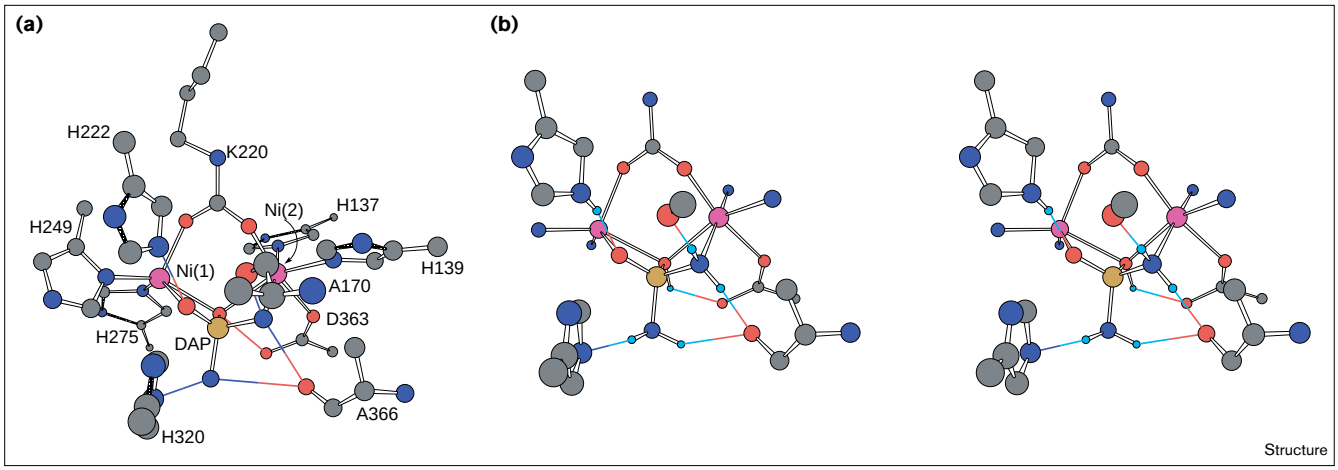


Refined model of the active site of DAP-inhibited BPU. **(a)** The coordination of the nickel ions and the DAP-binding mode are shown. **(b)** Stereoview of the DAP-inhibited BPU active site hydrogen-bonding network. Explicit hydrogen atoms are shown in positions that were calculated taking into account the geometric constraints, determined by the structure, on the DAP atoms. The colour scheme is identical to that used in Figure 4.

the protons on the distal nitrogen in DAP-inhibited BPU. In the latter case, the closing of the flap has caused the displacement of the sulphate ion by His$^{\alpha 323}$ (see Figures 4 and 7) which then acts as hydrogen-bonding acceptor as a result of the presence of a hydrogen bond between His$^{\alpha 323}$ Nδ and Asp$^{\alpha 224}$ Oδ2 (2.9 Å).

### The active-site residues in the 'open' and 'closed' flap conformations

The direct observation of an 'open' conformation in native BPU, and of a 'closed' flap in DAP-inhibited BPU, allows analysis of the effects caused by this conformational change on the position of the amino acid sidechains lining the active-site cavity. In both structures, the positions of conserved amino acid residues not involved in nickel binding but thought to be important in the catalytic mechanism (Ala$^{\alpha 170}$, His$^{\alpha 222}$, Gly$^{\alpha 280}$, Cys$^{\alpha 322}$, His$^{\alpha 323}$, His$^{\alpha 324}$, Arg$^{\alpha 339}$ and Ala$^{\alpha 366}$) are largely invariant, except for Cys$^{\alpha 322}$, His$^{\alpha 323}$, His$^{\alpha 324}$ and Arg$^{\alpha 339}$ (Figure 2). In particular, in native BPU (open conformation) His$^{\alpha 323}$ is displaced by approximately 5 Å from its position in DAP-inhibited BPU (closed conformation, compare Figures 4 and 7). The opening of the flap in native BPU also induces a large shift of the position of Cys$^{\alpha 322}$ (~4 Å) and of His$^{\alpha 324}$ (~7 Å), located at the entrance and on the edge of the active-site cleft opening, respectively, with respect to their position when the flap is closed (as in DAP-inhibited BPU). Furthermore, in the latter case the carbonyl oxygen of Ala$^{\alpha 366}$ is at hydrogen-bonding distance from the DAP amido group bound to Ni(2) (located in a position corresponding to W(2) in native BPU), whereas, when the flap is open, the corresponding residue Ala$^{\alpha 366}$ is rotated away, at a distance (5.1 Å from W(2)) that does not allow the formation of hydrogen bonds (compare Figures 4 and 7). The position of the sidechain of Arg$^{\alpha 339}$, stretching from the very bottom of the cleft toward the active site nickel ions, is not influenced as much as for Cys$^{\alpha 322}$, His$^{\alpha 323}$ and His$^{\alpha 324}$ by the flap opening, which induces a shift of the terminal guanidinium group of only approximately 1 Å away from the nickel ions with respect to its position in DAP-inhibited BPU.

### A proposal for the mechanism of urease

The currently accepted view of the mechanism of urease is based on different roles played by the two nickel ions: one of them binding and activating urea, the other binding and activating the nucleophile water molecule [1,2,11,31]. In particular, in view of the crystal structure of KAU and of its mutants, it was proposed that urea binds to the five-coordinate Ni(1) while the hydroxide ion, bound to the hexa-coordinate Ni(2), acts as nucleophile [1,2]. This model entails a reaction intermediate which would bridge the two nickel ions in a bidentate mode through two O atoms. This mechanism raises two problems, however [2]. One concerns the missing general base with $pK_a$ 9.0 [25,31–33] which would deprotonate the Ni(2)-bound water molecule ($pK_a$ = 10.6) at the optimum pH for enzyme activity (pH 8), and the second concerns the role of His$^{\alpha 323}$ as a general acid, which must be protonated at pH 8 even though it has a $pK_a$ of 6.5 [34,35]. These inconsistencies forced the introduction of the 'reverse protonation' hypothesis [2], which would, however, result in only 0.3% of all urease molecules being in the optimal protonation state for catalysis.

The crystal structures of native and DAP-inhibited BPU provide new information about the enzyme in the resting

**Figure 8**

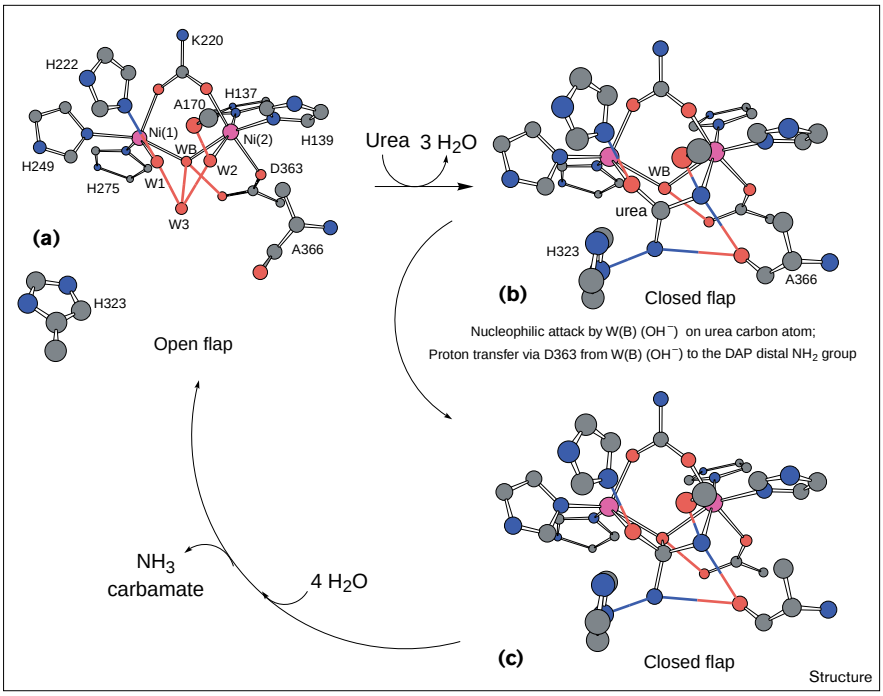


A proposed mechanism for urease. Only the essential atoms of the nickel ligands and of relevant amino acids involved in the mechanism are shown. Hydrogen bonds are coloured according to the CPK colours of the atoms involved. **(a)** Model of the resting enzyme taken from the crystal structure of native BPU. **(b)** Proposed urea-binding mode, obtained by modelling the substrate into the cavity of the DAP-inhibited BPU. **(c)** Model for the transition state of urea hydrolysis built from the crystal structure of DAP-inhibited BPU.

state and in a complex with a transition-state analogue. The results presented here prompt us to propose a novel mechanism. The presence of the tetrahedral water/hydroxide cluster in the proximity of the dinickel center in the structure of native BPU, together with the binding mode of DAP, suggest an enzyme active site accurately designed to selectively bind the substrate in an orientation-specific mode, and subsequently to stabilize a tetrahedral transition state. According to our proposal, urea enters the active-site cavity when the flap is in the open conformation, replacing W(1), W(2), and W(3), which are located in positions matching its molecular shape and dimensions. The hydrogen-bonding network, which stabilizes the binding of DAP to the active site, orientates the substrate in the catalytic cavity. Urea binds the more electrophilic five-coordinated Ni(1) with the carbonyl oxygen, approaching the six-coordinated Ni(2) with one of its amino groups and eventually bridging the two metal ions (Figure 8a,b). The protonation state of $His^{\alpha 222}$ Nε stabilizes the binding of the urea carbonyl O atom to Ni(1). Furthermore, the conformational change from the open to the closed position of the flexible flap induces a rearrangement of $Ala^{\alpha 366}$ carbonyl group such that its oxygen atom points towards Ni(2) (Figure 8b). The carbonyl groups of $Ala^{\alpha 170}$ and $Ala^{\alpha 366}$ are therefore now positioned to act as hydrogen-bond acceptors towards the urea $NH_2$ group, thereby assisting its binding to Ni(2). Urea is a poor chelating ligand because of the low Lewis base character of its $NH_2$ groups; the hydrogen bonds with the nearby carbonyl oxygens of $Ala^{\alpha 170}$ and $Ala^{\alpha 366}$ would, however, enhance the basicity of the amino group and facilitate its binding to Ni(2). An analogous effect has already been observed in the chelating binding mode of β-ME to the active site of BPU [17]. In conclusion, the orientation of the substrate is induced by the asymmetric structural features of the active-site residues, positioned to act as hydrogen-bond donors in the vicinity of Ni(1) and as hydrogen-bond acceptors in the vicinity of Ni(2).

The bidentate ligation of urea to the two very electrophilic nickel ions, together with the hydrogen-bonding network described, strongly activates the inert urea molecule towards nucleophilic attack, by polarizing the C–O and the C–$NH_2$ bonds. This binding mode of the substrate brings the carbon atom of urea in close proximity to the nickel-bridging ligand, proposed here to be the nucleophile in the form of a hydroxide anion (Figure 8b,c). Analogously, this process can also be described as an electrophilic attack of the activated urea carbon atom on the nickel-bridging hydroxide, in turn activated by the hydrogen bond with $Asp^{\alpha 363}$, which increases its partial negative charge. In the closed conformation, $His^{\alpha 323}$ appears to be in the proper position to interact with the transition state/product of the reaction as shown in Figure 8c. The tetrahedral transition state, formed upon bond formation between the nickel-bridging hydroxide and the urea carbon atom, is mimicked by DAP. In this process, $His^{\alpha 222}$ and $His^{\alpha 323}$ act by stabilizing, respectively, the negative and

positive charges developing on the tetrahedral intermediate. The proton needed by the distal urea $NH_2$ group in order to induce cleavage of the C–N bond and release of ammonia could easily be provided by the hydroxide nucleophile itself, the $pK_a$ of which is decreased by the formation of the C–O bond. This transfer is possibly assisted by the carboxylate group of $Asp^{\alpha 363}$. In the closed conformation of the flap, $His^{\alpha 323}$ is placed at hydrogen-bonding distance from the nascent ammonia (Figure 8b,c). In the final step, the DAP C–N bond is broken, and ammonia is released from the active site, assisted by the movement of $His^{\alpha 323}$ when the flexible flap opens. The resulting negatively charged carbamate is then released, owing to the unfavourable interaction between the deprotonated nickel-bridging carbamate oxygen and $Asp^{\alpha 363}$ Oδ2, in a process assisted by the movement of the positively charged $Arg^{\alpha 339}$ upon flap opening.

The mechanism proposed here overcomes the problems encountered by the currently most accepted mechanism suggested by others [1,2,11,31]: the bridging hydroxide is considered to be both the nucleophile and the general acid, while $His^{\alpha 323}$ acts as a general base, not by deprotonating the hydrolytic water, but by stabilizing the positive charge which develops on the transition state. Our model is also consistent both with a role in substrate binding for $His^{\alpha 222}$ [34] and with the pH dependence of $k_{cat}$, featuring apparent $pK_a$ values near 6.5 and 9 [25,31–33]. The latter $pK_a$, still not assigned to any active-site residues, is attributed here to the deprotonation of the bridging hydroxide anion, the hydrogen of which is needed, according to our model, to protonate the distal amido group and yield ammonia. Furthermore, the proposed transition-state binding mode is consistent with a binding energy larger than 19 kcal/mol, as demanded by an enzyme proficiency greater than $10^{14}$ [2], because the proposed binding of the transition state involves four coordination bonds to the nickel ions and six hydrogen-bonding interactions. Finally, the structure of DAP-inhibited BPU suggests a binding mode for the transition state analogue that is not consistent with the mechanism proposed by others [1,2,11,31], because of the presence of an oxygen atom of DAP bridging the two nickel ions, and so excluding the possibility that the two substrates, urea and water, initially reside on two different nickel ions.

Our model provides a rationale for the presence of a bimetallic active site in urease, as well as explaining the requirement for nickel ions, in place of the more common zinc ion in hydrolytic enzymes. Nickel ions are characterized by higher affinity for nitrogen-based ligands than zinc ions [36], thereby stabilizing the binding of a urea $NH_2$ group. In addition, the presence of a bimetallic center, with the nickel ions having multiple available binding sites because of their preference for octahedral coordination sphere (as opposed to zinc ions, mostly tetrahedral), would represent a requirement for both the bridging–binding mode of urea and for stabilization of the metal ion binding to the protein through multiple sites for amino acid ligands.

It has recently been pointed out that the overall architecture of urease reveals striking similarities to other enzymes, such as adenosine deaminase, dihydro-orotases, allantoinases, hydantoinases, AMP deaminase, adenine deaminase, cytosine deaminase, imidazolonepropionase, aryldialkylphosphatases, chlorohydrolase, formylmethanefuran dehydrogenases, and proteins involved in animal neuronal development [37]. In addition to the common core made of an $(\alpha\beta)_8$ barrel, all these proteins share similar properties such as the role of metal ion(s) in activating a water molecule toward nucleophilic attack on the substrate, and the presence of a conserved metal-binding site at the C-terminal end of strands $\beta_1$, $\beta_5$, $\beta_6$, and $\beta_8$. In this context, the novel mechanistic model proposed here for urease, the central feature of which is the role of the metal-bridging hydroxide acting as the nucleophile, is analogous to that suggested for other bimetallic hydrolases such as phospholipase C ($Zn_2$) [38], leucine aminopeptidase ($Zn_2$) [39], arginase ($Mn_2$) [40], inorganic pyrophosphatase ($Mg_2$) [41], aryldialkylphosphatase ($Zn_2$) [42], and proline aminopeptidase ($Mn_2$) [43], and purple acid phosphatase ($Fe_2$ or FeZn) [44] even though only for leucine aminopeptidase is this mechanism supported by the crystal structure of an enzyme–intermediate complex. Such a mechanistic role for the hydroxide-bridged bimetallic core may well constitute a general model for all hydrolytic enzymes containing similar catalytic sites [45]. The present detailed description of the active site in native BPU and BPU inhibited by a transition state analogue therefore leads to precise predictions for the mechanism of action of a broad ensemble of evolutionarily distant enzymes.

## Biological implications

**Urea is formed in large quantities as a product of the catabolism of nitrogen-containing compounds, each human producing approximately 10 kg of urea per year. Although the spontaneous degradation of urea has a half-life of approximately 3.6 years [11], urea hydrolysis catalyzed by urease (urea aminohydrolase E.C. 3.5.1.5), a nickel-containing enzyme [46], proceeds $10^{14}$ times faster [47]. The products of this reaction are ammonia and carbamate: the latter spontaneously decomposes to ammonia and carbonate in an uncatalysed reaction [33,47–49].**

**The balanced hydrolysis of the reaction products causes an increase in pH, a negative side-effect of the action of urease both for human and animal health and for agriculture. Urease activity is involved in urolithiasis, catheter encrustation, pyelonephritis, ammonia and hepatic encephalopathy, hepatic coma, urinary tract infections, and is known to be the major cause of pathologies (including cancer) induced by gastroduodenal infections**

by *Helicobacter pylorii* [33,49]. High urease activity in the soil causes significant environmental and economic problems by releasing large amounts of ammonia into the atmosphere during nitrogen fertilization with urea (the most used fertilizer world-wide), further inducing plant damage by ammonia toxicity and increase in the pH of soil [33,50].

The control of urea hydrolysis by use of urease inhibitors would lead to a reduction in environmental pollution, enhanced efficiency of urea nitrogen uptake by plants, and improved therapeutic strategies for the treatment of infections due to ureolytic bacteria. Several classes of molecule have been tested as urease inhibitors both in medicine [49] and in agriculture [50]. The efficiency of the presently available inhibitors is low, however, and negative side effects on humans [33,49] and on the environment [33,51] have been reported.

The discovery of urease inhibitors has to date relied upon extended screen tests [52]. The high-resolution structure of native and inhibited urease from *B. pasteurii* provides experimental evidence for a novel mechanism of urea hydrolysis, thereby paving the way for the reliable structure-based design of efficient inhibitors, currently in progress in our laboratory. The structural similarity with other dinuclear metallo-hydrolases suggest analogous mechanistic aspects for evolutionarily distant hydrolytic enzymes.

## Materials and methods

*Protein purification and crystallization*

BPU was isolated and purified to a specific activity of ~2500 units/mg [13]. Crystallisation of the native enzyme was performed at 20°C by the 'hanging drop method', using 3 µl of 11 mg/ml BPU solution in 20 mM Tris-HCl, pH 7.5, containing 50 mM $Na_2SO_3$, and diluting this volume with 3 µl of precipitant solution (a saturated ammonium sulphate solution containing 1.2 M LiCl, diluted to 53% using 20 mM sodium citrate, pH 6.3). Colourless crystals grew to about $0.2 \times 0.2 \times 0.6$ mm in 4 days. The crystals were 'rice shaped', exhibiting sharply defined faces and hexagonal bipyramidal geometry only rarely [14].

Crystallization of PPD-inhibited BPU was achieved at 20°C using the same protein solution as above, exchanged with a solution of 20 mM Tris-HCl, pH 8.0, containing 4 mM PPD. A solution containing 100 mM sodium citrate, pH 6.3, 1.9 M ammonium sulphate, and 4 mM PPD, was used as precipitant. Well-shaped colourless single crystals, having the same habit as for the native form, grew to about $0.2 \times 0.2 \times 0.5$ mm in 4 days.

*Data collection and evaluation*

Diffraction data were collected on a single crystal of the native protein at 100K using synchrotron radiation from the BW7B wiggler line of the DORIS storage ring at the EMBL outstation at the Deutsches Elektronen Synchrotron (DESY) in Hamburg (Germany), using a 30 cm MarResearch imaging plate scanner as previously described [14]. For cryoprotection, a single crystal of inhibited BPU, of dimensions $0.2 \times 0.2 \times 0.4$ mm, was transferred from the crystallization drop into 500 µl soaking solution (2.4 M ammonium sulphate, 4 mM PPD, 100 mM sodium citrate, pH 6.3). The concentration of the cryoprotectant was gradually increased from 0 to 15% by adding 100 µl portions of 20% ethylene glycol, at 1 min intervals. The crystal was transferred to a soaking solution containing 20% ethylene glycol and, after 1 min, it was scooped up in a cryo-loop and rapidly exposed to a cold nitrogen stream.

**Table 2**

**X-ray data collection statistics and summary of the crystallographic analysis.**

| | Native BPU | DAP-inhibited BPU |
|---|---|---|
| Resolution range (Å) | 20.00–2.00 | 18.00–2.00 |
| $R_{merge}$* | 0.097 | 0.150 |
| Raw measurements | 836,977 | 874,166 |
| Unique reflections | 63,765 | 65,301 |
| Redundancy | 13.1 | 13.4 |
| Completeness (%) | 96.7 | 99.9 |
| Completeness (%) | 95.4 | 99.9 |
| (high resolution bin (Å)) | (2.02–2.00) | (2.04–2.00) |
| Greater than 3σ (%) | 70.2 | 67.4 |
| I/σ in high resolution bin | 2.4 | 2.8 |
| Space group | $P6_322$ | $P6_322$ |
| $a = b$ (Å) | 131.36 | 131.53 |
| $c$ (Å) | 189.76 | 188.45 |
| Protein atoms | 6054 | 6054 |
| Solvent atoms | 881 | 841 |
| Bound metal ions | 2 Ni | 2 Ni |
| Temperature factors | | |
| for protein atoms (Å$^2$) | 19.3 | 14.2 |
| for solvent (Å$^2$) | 34.0 | 27.8 |
| for Ni(1), Ni(2) (Å$^2$) | 19.1, 17.9 | 21.2, 16.8 |
| Rms bond length deviation (Å) | 0.013 | 0.009 |
| Rms bond angle deviation (Å) | 0.028 | 0.028 |
| Rms planes deviation (Å) | 0.033 | 0.033 |
| Ramachandran plot | | |
| allowed region (%) | 89.6 | 89.0 |
| additional allowed region (%) | 10.3 | 10.8 |
| R factor ($R_{free}$)† (%) | 16.2 (20.4) | 15.8 (20.0) |

*$R_{merge} = \Sigma|I^i - \langle I\rangle|/\Sigma\langle I\rangle$, where $I^i$ is an individual intensity measurement, and $\langle I\rangle$ is the average intensity for this reflection with summation over all the data. †R factor $= \Sigma\, ||F_o| - |F_c||/\Sigma|F_o|$; R factor and $R_{free}$ are calculated by using the working and free reflection sets, respectively, the free reflections (2% of the total) were held aside throughout the refinement. Rms, root mean square.

The data were processed using the program DENZO and merged with SCALEPACK [53]. Table 2 reports a summary of data collection statistics and data reduction for both native and inhibited BPU.

*Structure determination and refinement*

Initial phases for both native and inhibited BPU were obtained from the refined model of the isomorphous β-ME-inhibited enzyme (PDB code 1UBP [17]). The protein regions displaying different conformations were manually rebuilt with the program O [54]. The initial model for the DAP molecule was obtained using the program Chem3D.

The structures of native and inhibited BPU were refined using a sequence of PROLSQ [55,56] and REFMAC [57] cycles with established geometric targets [58]. No restraints were used for the nickel–ligand distances. Water molecules were inserted and refined using the program ARP, keeping only those water molecules having density greater than 1.3σ in the electron-density map [59]. The omit maps were calculated after several refinement cycles of a model from which the four water/hydroxide molecules cluster, or the DAP atoms, were omitted. Table 2 reports the final refinement parameters. The stereochemistry of the final models were checked by using the programs WHATIF [60] and PROCHECK [61].

*Accession numbers*

The refined crystallographic coordinates for native and DAP-inhibited BPU have been deposited in the Brookhaven Protein Data Bank under accession codes 2UBP and 3UBP, respectively.

## Acknowledgements

The authors acknowledge fundings from the European Union (for support of the work at EMBL Hamburg through the HCMP Access to Large Installation Projects, Contract Number CHGE-CT93-0040), from the Italian Consiglio Nazionale delle Ricerche (Comitato 11 Tecnologia e Innovazione (to SC)), from the Ministero dell'Università e della Ricerca Scientifica e Tecnologica – MURST. (Fondi ex-40% to SC and SM), and from EMBL (predoctoral fellowship to SB).

## References

1. Jabri, E., Carr, M.B., Hausinger, R.P. & Karplus, P.A. (1995). The crystal structure of urease from *Klebsiella aerogenes*. *Science* **268**, 998-1004.
2. Karplus, P.A., Pearson, M.A. & Hausinger, R.P. (1997). 70 years of crystalline urease: what have we learned? *Acc. Chem. Res.* **30**, 330-337.
3. Wang, S., Lee, M.H., Hausinger, R.P., Clark, P.A., Wilcox, D.E. & Scott, R.A. (1994). Structure of the dinuclear active site of urease. X-ray absorption spectroscopic study of native and 2-mercaptoethanol-inhibited bacterial and plant enzymes. *Inorg. Chem.* **33**, 1589-1593.
4. Blakeley, R.L., Dixon, N.E. & Zerner, B. (1983). Jack bean urease. VII. Light scattering and nickel(II) spectrum. Thiolate-nickel(II) charge transfer peaks in the spectrum of the β-mercaptoethanol-urease complex. *Biochim. Biophys. Acta* **744**, 219-229.
5. Hasnain, S.S. & Piggot, B. (1983). An EXAFS study of jack bean urease, a nickel metalloenzyme. *Biochem. Biophys. Res. Commun.* **112**, 279-283.
6. Alagna, L., Hasnain, S.S., Piggot, B. & Williams, D.J. (1984). The nickel ion environment in jack bean urease. *Biochem. J.* **220**, 591-595.
7. Clark, P.A. & Wilcox, D.E. (1989). Magnetic properties of the nickel enzyme urease, nickel-substituted carboxypeptidase A, and nickel-substituted carbonic anhydrase. *Inorg. Chem.* **28**, 1326-1333.
8. Clark, P.A., Wilcox, D.E. & Scott, R.A. (1990). X-ray absorption spectroscopic evidence for binding of the competitive inhibitor 2-mercaptoethanol to the nickel sites of jack bean urease. A new Ni-Ni interaction in the inhibited enzyme. *Inorg. Chem.* **29**, 579-581.
9. Finnegan, M.G., Kowal, A.T., Werth, M.T., Clark, P.A., Wilcox, D.E. & Johnson, M.K. (1991). Variable temperature magnetic circular dichroism spectroscopy as a probe of the electronic and magnetic properties of nickel in jack bean urease. *J. Am. Chem. Soc.* **113**, 4030-4032.
10. Benini, S., Ciurli, S., Nolting, H.F. & Mangani, S. (1996). X-ray absorption spectroscopy study of native and phenylphosphorodiamidate-inhibited *Bacillus pasteurii* urease. *Eur. J. Biochem.* **239**, 61-66.
11. Zerner, B. (1991). Recent advances in the chemistry of an old enzyme, urease. *Bioorg. Chem.* **19**, 116-131.
12. Pearson, M.A., Overbye Michel, L., Hausinger, R.P. & Karplus, P.A. (1997). Structures of Cys319 variants and acetohydroxamate-inhibited *Klebsiella aerogenes* urease. *Biochemistry* **36**, 8164-8172.
13. Benini, S., Gessa, C. & Ciurli, S. (1996). *Bacillus pasteurii* urease: an heteropolymeric enzyme with a binuclear nickel active site. *Soil Biol. Biochem.* **28**, 819-821.
14. Benini, S., Ciurli, S., Rypniewski, W., Wilson, K.S. & Mangani, S. (1998). Crystallization and preliminary high resolution X-ray diffraction analysis of native and β-mercaptoethanol-inhibited urease from *Bacillus pasteurii*. *Acta Crystallogr. D* **54**, 409-412.
15. Moersdorf, G., Weinmann, P. & Kaltwasser, H. (1994), EMBL Data Library, X78411.
16. Mulrooney, S.B. & Hausinger, R.P. (1990). Sequence of the *Klebsiella aerogenes* urease genes and evidence for accessory proteins facilitating nickel incorporation. *J. Bacteriol.* **172**, 5837-5843.
17. Benini, S., Rypniewski, W.R., Wilson, K.S., Ciurli, S. & Mangani, S. (1998). The complex of *Bacillus pasteurii* urease with β-mercaptoethanol from X-ray data at 1.65 Å resolution. *J. Biol. Inorg. Chem.* **3**, 268-273.
18. Dixon, N.E., Gazzola, C., Watters, J.J., Blakeley, R. & Zerner, B. (1975). Inhibition of jack bean urease (EC 3.5.1.5) by acetoxydroxamic acid and by phosphoramidate. An equivalent weight for urease. *J. Am. Chem. Soc.* **97**, 4130-4131.
19. Dixon, N.E., Blakeley, R.L. & Zerner, B. (1980). Jack bean urease (E.C. 3.5.1.5). III. The involvement of active-site nickel ion in inhibition by β-mercaptoethanol, phosphoramidate, and fluoride. *Can. J. Biochem.* **58**, 481-488.
20. Todd, M.J. & Hausinger, R.P. (1989). Competitive inhibitors of *Klebsiella aerogenes* urease. Mechanisms of interaction with the nickel active site. *J. Biol. Chem.* **264**, 15835-15842.
21. McCarthy, G.W., Bremner, J.M. & Lee, J.S. (1990). Inhibition of plant and microbial ureases by phosphoramides. *Plant Soil* **127**, 269-283.
22. Moncrief, M.B.C., Hom, L.G., Jabri, E., Karplus, P.A. & Hausinger, R.P. (1995). Urease activity in the crystalline state. *Protein Sci.* **4**, 2234-2236.
23. Allen, F.H. & Kennard, O. (1993). 3D search and research using the Cambridge Structural Database. *Chemical Design Automation News* **8**, 31-37.
24. Basolo, F. & Pearson, R.G. (1967). Acid-Base Properties of Complex Ions In *Mechanisms of Inorganic Reactions*, pp. 31-33, Wiley, New York,
25. Ciurli, S., Marzadori, C., Benini, S., Deiana, S. & Gessa, C. (1996). Urease from the soil bacterium *Bacillus pasteurii*. 2. Immobilization on Ca-polygalacturonate. *Soil Biol. & Biochem.* **28**, 811-817.
26. Day, E.P., Peterson, J., Sendova, M.S., Todd, M.J. & Hausinger, R.P. (1993). Saturation magnetization of ureases from *Klebsiella aerogenes* and jack bean: no evidence for exchange coupling between the two active site nickel ions in the native enzymes. *Inorg. Chem.* **32**, 634-638.
27. Park, I.-S., *et al.*, & Hausinger, R.P. (1996). Characterization of the mononickel metallocenter in H134A mutant urease. *J. Biol. Chem.* **271**, 18632-18637.
28. Pearson, M.A., Schaller, R.A., Michel, L.O., Karplus, P.A. & Hausinger, R.P. (1998). Chemical rescue of *Klebsiella aerogenes* urease variants lacking the carbamylated-lysine nickel ligand. *Biochemistry* **37**, 6214-6220.
29. Jeffrey, G.A. & Saenger, W. (1991). Metrical Aspects of Three- and Four-Center Hydrogen bonds In *Hydrogen Bonding in Biological Structures*, p. 18, Springer-Verlag, Berlin.
30. Andrews, R.K., Dexter, A., Blakeley, R.L. & Zerner, B. (1986). Jack bean urease (EC 3.5.1.5). VIII. On the inhibition of urease by amides and esters of phosphoric acid. *J. Am. Chem. Soc.* **108**, 7124-7125.
31. Dixon, N.E., Riddles, P.W., Gazzola, C., Blakeley, R.L. & Zerner, B. (1980). Jack bean urease. V. On the mechanism of action of urease on urea, formamide, acetamide, N-methylurea, and related compounds. *Can. J. Biochem.* **58**, 1335-1345.
32. Todd, M.J. & Hausinger, R.P. (1987). Purification and characterization of the nickel-containing multicomponent urease from *Klebsiella aerogenes*. *J. Biol. Chem.* **262**, 5963-5967.
33. Mobley, H.L.T. & Hausinger, R.P. (1989). Microbial urease: significance, regulation and molecular characterization. *Microbiol. Rev.* **53**, 85-108.
34. Park, I.-S. & Hausinger, R.P. (1993). Site-directed mutagenesis of *Klebsiella aerogenes* urease: identification of hystidine residues that appear to function in nickel ligation, substrate binding, and catalysis. *Protein Sci.* **2**, 1034-1041.
35. Park, I.-S. & Hausinger, R.P. (1993). Diethylpyrocarbonate reactivity of *Klebsiella aerogenes* urease: effect of pH and active site ligands on the rate of inactivation. *J. Protein Chem.* **12**, 51-56.
36. Smith, R.M. & Martell, A.E. (1975). In *Critical Stability Constants*, Volume 2: Amines, Plenum Press, New York and London.
37. Holm, L. & Sander, C. (1997). An evolutionary treasure: unification of a broad set of amidohydrolases related to urease. *Proteins* **28**, 72-82.
38. Sundell, S., Hansen, S. & Hough, E. (1994). A proposal for the catalytic mechanism in phospholipase C based on interaction energy and distance geometry calculations. *Protein Eng.* **7**, 571-577.
39. Strater, N. & Lipscomb, W.N. (1995). Two-metal ion mechanism of bovine lens leucine aminopeptidase: active site solvent structure and binding mode of L-leucinal, a gem-diolate transition state analogue, by X-ray crystallography. *Biochemistry* **34**, 14792-14800.
40. Kanyo, Z.F., Scolnick, L.R., Ash, D.E. & Christianson, D.W. (1996). Structure of a unique binuclear manganese cluster in arginase. *Nature* **283**, 554-557.
41. Heikinheimo, P., *et al.*, & Lahti, R. (1996). A site-directed mutagenesis study of *Saccharomyces cerevisiae* pyrophosphatase. Functional conservation of the active site of soluble inorganic pyrophosphatases. *Eur. J. Biochem.* **239**, 138-143.
42. Vanhooke, J.L., Benning, M.M., Raushel, F.M. & Holden, H.M. (1996). Three-dimensional structure of the zinc-containing phosphotriesterase with the bound substrate analog diethyl 4-methylbenzylphosphonate. *Biochemistry* **35**, 6020-6025.

43. Wilce, M.C.J., *et al*., & Wilce, J.A (1998). Structure and mechanism of a proline-specific aminopeptidase from *Escherichia coli*. *Proc. Natl Acad. Sci. USA* **95**, 3472-3477.
44. Wang, X., Randall, C.R., True, A.H. & Que, l.Jr. (1996). X-ray absorption spectroscopic studies of the FeZn derivative of uteroferrin. *Biochemistry* **35**, 13946-13954.
45. Wilcox, D.E. (1996). Binuclear metallohydrolases. *Chem. Rev.* **96**, 2435-2458.
46. Dixon, N.E., Gazzola, C., Blakeley, R. & Zerner, B. (1975). Jack bean urease (EC 3.5.1.5). A metalloenzyme. A simple biological role for nickel? *J. Am. Chem. Soc.* **97**, 4131-4132.
47. Hausinger, R.P. (1993). *Biochemistry of Nickel*, Plenum Press, New York.
48. Andrews, R.K., Blakeley, R.L. & Zerner, B. (1989). Urease - A Ni(II) Metalloenzyme. In *The Bioinorganic Chemistry of Nickel* (Lancaster, J.R., Jr., ed.), pp. 141-166, VCH Publishers, Inc., New York, NY 10010.
49. Mobley, H.L.T., Island, M.D. & Hausinger, R.P. (1995). Molecular biology of microbial ureases. *Microbiol. Rev.* **59**, 451-480.
50. Bremner, J.M. (1995). Recent research on problems in the use of urea as a nitrogen fertilizer. *Fert. Res.* **42**, 321-329.
51. Krogmeier, M.J., McCarty, G.W. & Bremner, J.M. (1989). Potential phytotoxicity associated with the use of soil urease inhibitors. *Proc. Natl Acad. Sci. USA* **86**, 1110-1112.
52. Hamilton-Miller, J.M.T. & Gargan, R.A. (1979). Rapid screening for urease inhibitors. *Invest. Urol.* **16**, 327-328.
53. Otwinowski, Z. & Minor, W. (1997). Processing of X-ray diffraction data collected in oscillation mode. *Methods Enzymol. A* **276**, 307-325.
54. Jones, T.A., Zou, J.Y., Cowan, S.W. & Kjeldgaard, M. (1991). Improved methods for building protein models in electron density maps and the location of errors in these models. *Acta Cryst. A* **47**, 110-119.
55. Konnert, J.H. (1976). A restrained-parameter structure-factor least-squares refinement procedure for large asymmetric units. *Acta Crystallogr. A* **32**, 614-617.
56. Konnert, J.H. & Hendrickson, W.A. (1980). A restrained-parameter thermal-factor refinement procedure. *Acta Crystallogr. A* **36**, 344-350.
57. Murshudov, G.N., Vagin, A.A. & Dodson, E.J. (1997). Refinement of macromolecular structures by the maximum-likelihood method. *Acta Cryst. D* **53**, 240-255.
58. Engh, R.A. & Huber, R. (1991). Accurate bond and angle parameters for X-ray protein structure refinement. *Acta Crystallogr. A* **47**, 392-400.
59. Lamzin, V.S. & Wilson, K.S. (1997). Automated refinement for protein crystallography. *Methods Enzymol.* **277**, 269-305.
60. Vriend, G. (1990). WHATIF: a molecular modelling and drug design program. *J. Molec. Graph.* **8**, 52-56.
61. Laskowski, R.A., MacArthur, M.W., Moss, D.S. & Thornton, J.M. (1993). PROCHECK: a program to check the stereochemical quality of protein structures. *J. Appl. Crystallogr.* **26**, 283-291.


**Because *Structure with Folding & Design* operates a 'Continuous Publication System' for Research Papers, this paper has been published on the internet before being printed (accessed from http://biomednet.com/cbiology/str). For further information, see the explanation on the contents page.**